Edinburgh Research Explorer

A discrete element model for orogenesis and accretionary wedge growth

A discrete element model for orogenesis and accretionary wedge growth

M. Naylor and H. D. Sinclair

School of GeoSciences, University of Edinburgh, Edinburgh, UK

S. Willett

Department of Earth and Space Sciences, University of Washington, Seattle, Washington, USA

P. A. Cowie

School of GeoSciences, University of Edinburgh, Edinburgh, UK

[1]   We develop a two-dimensional discrete element model to investigate the evolution of doubly vergent orogenic and accretionary wedges. This generates the localization of deformation across persistent structures as emergent phenomena unlike many continuum models that require predefined weaknesses to localize strain. The model is used to study how deformation processes evolve for two different boundary conditions, drawing strong comparisons with previous sandbox analogues and computational approaches. The deformational history of the modeled wedges is characterized by three stages defined by an evolution in the mechanisms available to accommodate shortening. The first stage develops a strong retrovergent thrust that initiates at the subduction point; the second stage shows a change in vergence of deformation as thin-skinned thrusting propagates into material carried on the subducting plate thus evolving a folded and thrusted prowedge; finally, a second shallower retrowedge develops in the overriding plate through accretion. This final stage is not present in all sand analogue modeling approaches, and defines a difference in the deformation style. Thresholds in geometry and size regulate the localization and style of deformation and hence the progression through the three stages. The wedges produced show periodicity in the modes of accretion to maintain a geometric form, with deformation localizing across structures that are internally reactivated. Thus prowedges and retrowedges are seen to oscillate about constant taper angles.

1. Introduction

[2]   The long-term ($10^6 - 10^7$ years) mechanical growth of mountain belts was first investigated through detailed mapping and dating of rocks in mountain belts such as the European Alps and North American Rockies. The recognition of crustal thickening was identified when the first thrust faults were documented [*Heim*, 1897], and later quantified by the study of negative gravity anomalies formed by isostatic compensation of the thickened crust [*Karner and Watts*, 1983]. Once these observations had been integrated into a mechanical interpretation for the macroscale form of mountain belts as a thrust wedge [*Chapple*, 1978], the foundations for numerical and analogue modeling of mountain systems were available. However, the expansive understanding of mountain belts as we see them today provides us with a snapshot in time, and even then it can be difficult to resolve internal structures. In order to further investigate the evolution of orogens, forward modeling is required to make predictions and to define possible endpoint scenarios that can be tested against real data to better improve assumptions used in modeling.

[3]   Currently, orogens are modeled through both sand analogues [*Malavieille*, 1984; *Storti et al.*, 2000; *Persson*, 2001] and numerical finite element techniques [*Willett et al.*, 1993; *Beaumont et al.*, 1996]. They identify similar evolutionary schemes, but differ in the type of detail they can resolve, boundary conditions and model parameterization. Sandbox models generate individual structures but are limited by the range of parameter space available and experimental repeatability. Finite element models have an appropriate gross parameterization but their Coulomb continuum assumption excludes discrete thrusting and shear surface formation. Numerous examples exist where modeling has enhanced our understanding on the controls on orogenic evolution. For example, finite element models (FEMs) have demonstrated the kinematic significance of inherited crustal heterogeneities during growth of the Pyrenees [*Beaumont et al.*, 2000]. Similarly, sandbox experi-
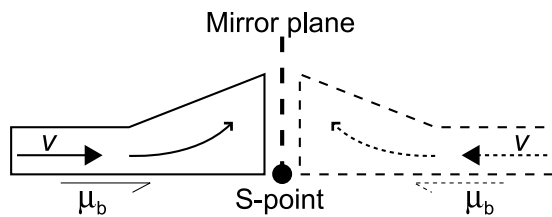
Figure 1. A kinematic comparison between critical wedge and doubly vergent wedge boundary conditions in a frame of reference with a stationary subduction point, the S point. The only way to satisfy the zero friction on the vertical backstop boundary condition in generalizing the singly vergent wedge to a doubly vergent context is for the system to be symmetric about the backstop, indicated by the dashed line mirror plane; v is the convergence rate at which material is introduced into the system from infinity, μ_b is the basal friction.

ments have demonstrated the importance of sediment blanketing on the growth accretionary wedges (e.g., the Mardin Formation in southeast Turkey [*Nieuwland et al.*, 2000]). Here, we outline an alternative method based upon a discrete element model (DEM) that combines appropriate parameterization for the macroscale form with the ability to accommodate shortening through discrete thrusting and shearing. The main developments from previous DEM modeling are (1) the use of more general particle packing structures, (2) the implementation of doubly vergent boundary conditions, and (3) the development of a Coulomb retroside boundary condition that produces shortening while still permitting Coulomb failure. This model is then used to investigate the essential components of the evolutionary development of orogens [*Willett et al.*, 1993] the relevance of which we consider in the context of specific geological settings. All of the results presented here are repeatable within some degree of variability that is introduced by the random seed of the initial packing.

[4] To model the evolution of orogens, we believe there are some first order observations that have to be respected. First, that the system forms a doubly vergent wedge with taper angles in the range of 2 to 10 degrees, higher angles are observed in sandbox analogues. Second, that the wedges grow by the accretion of individual thrust structures that may form imbricates and duplexes at the front, and on the base of the wedges. Third, that individual faults may have large offsets across them (hundreds to thousands of meters). Fourth, that the overriding plate also deforms and accretes material into the retrowedge.

2. Previous Modeling Approaches
2.1. Critical Wedge

[5] Critical wedge theory has been used to describe how accretionary prisms and fold and thrust belts oscillate about some constant taper angle and about their general form [*Chapple*, 1978; *Davis et al.*, 1983]. Strictly speaking, the angle is only critical if the system satisfies the critical wedge assumption; that material is at Coulomb failure everywhere, implying that it deforms as a continuum. However, a wedge may still maintain a constant taper angle, even if it is not generated through processes analogous to critical wedge accretion such as surficial mass

wasting, where the surface taper angle is some angle of repose of the material. Solutions have been presented for an infinite wedge of both a noncohesive [*Davis et al.*, 1983] and a cohesive [*Dahlen et al.*, 1984] Coulomb material as well as an exact analytic solution for the noncohesive critical wedge [*Dahlen*, 1984]. The critical taper angle of the wedge is a function of the internal strength of the material and the coefficient of friction on the basal detachment [*Willett*, 1992].

[6] *Huiqi et al.* [1992] used sandbox models to simulate the evolution of foreland fold and thrust belts. The models generated imbricate thrust sheets at the front of the wedge that became back-rotated in the more internal parts of the wedge. The tapers produced in the models were consistently higher than those predicted from theory. This is not surprising as sand is a granular material and as such extra phenomena, such as dilation and arching, play important roles that are not a component of critical taper theory. Despite this the wedges produced do try to sustain a constant taper angle.

[7] *Willett* [1992] successfully compared critical wedge theory using a finite element model (FEM) with the analytic solution of *Dahlen* [1984] and was able to investigate the response of the wedge to a change in basal friction. The critical wedge was modeled by advancing a rigid, vertical, smooth backstop into the deformable plastic Coulomb material. To approximate the infinite wedge, the taper angle is measured away from the backstop. The FEMs clearly demonstrated that deformation oscillates between internal thickening and frontal accretion to maintain the wedge taper and that weaker bases propagate information further away from the backstop generating shallower angles as compared with high basal frictions which localize uplift at the backstop.

[8] The continuum deformation implied by Coulomb failure at every point in a critical wedge formulation does not permit the development of structures with large, discrete offsets and strain partitioning as is observed in many thrust wedges. A system at Coulomb failure everywhere has no memory of recent sliding, only of the mass distribution and boundary conditions; a system which is only at Coulomb failure on discrete planes remembers recent deformation and has the option to reexploit this weakened zone.

[9] Two of the main problems with using a critical wedge as an analogue for orogenic evolution are, first, that the kinematic boundary conditions originally applied in critical wedge FEMs require a smooth backstop that equates to a system with both plates moving at the same velocity toward a singularity (Figure 1) [*Willett*, 1992]. Second, the critical wedge backstop is of infinite height, so there can be no transfer of material between the prosides and retrosides; material derived from the proside is observed in the retrowedge of many mountain belts. For example, the North Pyrenean Fault in the Pyrenees represents the suture zone between the colliding European and Iberian plates, but is now located approximately halfway down the retrowedge (northern) side of the mountain belt [*Munoz*, 1992]. Similar examples of the horizontal flux of material through the central divide of mountain belts from the prosides to the retrosides have been demonstrated from the Southern Alps in New Zealand and Cascades in Washington State [*Willett*, 1999]. Subsequent FEMs utilize a doubly vergent geometry
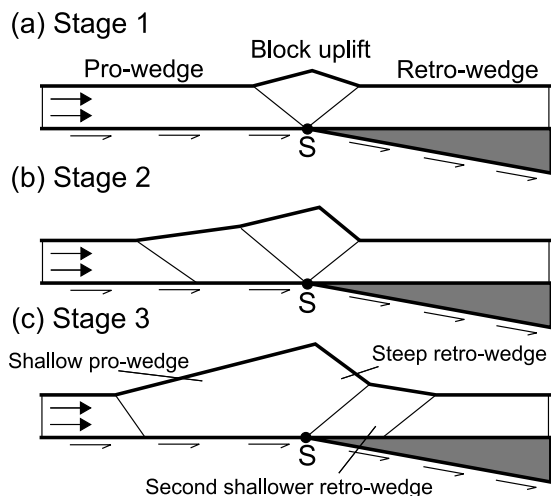
(a) Stage 1
Block uplift
Pro-wedge   Retro-wedge
S

(b) Stage 2
S

(c) Stage 3
Shallow pro-wedge   Steep retro-wedge
S
Second shallower retro-wedge

Figure 2. Illustration of the three characteristic stages in the evolution of a doubly vergent wedge. Modified from *Willett et al.* [1993].

and define the singularity as stationary with respect to the overriding plate; this is a more realistic boundary condition [*Willett et al.*, 1993].

[10] The strength of critical wedge theory concerns the dynamics and modes of accommodation of stress in the system. All things being equal, the slope will try to maintain a constant taper angle. If the wedge becomes too steep, it will slide stably on the base and accrete at the toe, to shallow the slope. If too shallow, material may be thrust under the wedge and be incorporated at the rear by underplating, causing a steepening of the wedge. If no material is added, the wedge can thicken internally, through processes analogous to back rotation of stacked imbricates, out-of-sequence thrusting and back thrusting [*Platt*, 1986]. The basal and internal coefficients of friction regulate the duration the system spends in each of these possible phases.

2.2. Doubly Vergent Wedges

[11] Here we outline the modeling approaches of several workers who have used a variety of sandbox and finite element approaches. They all improve upon critical wedge simulations for modeling real accretionary settings, by applying boundary conditions that are more geologically motivated.

[12] Doubly vergent wedges appear to follow an evolutionary scheme during their growth, involving three stages (Figure 2) [*Willett et al.*, 1993; *Storti et al.*, 2000]; these are characterized by the introduction of new deformation mechanisms that accommodate shortening. Stage 1 is characterized by the growth of a symmetric, steep sided topography about a central ridge. Deformation is dominated by motion along a retrovergent thrust and associated block uplift. There is no sliding along the base and material is fluxed to the S point. In stage 2 the wedge has now reached a threshold size where prowedge accretion occurs and the prowedge angle, and hence surface slope, is now dependent on the proside basal coefficient of friction; the wedge can now propagate stably on the proside. At stage 3, a further threshold is reached, a component of shortening is accommodated by stable sliding of the whole wedge on the prosides and retrosides, and material is accreted at the toe

of the steep retrowedge, forming a second, shallower wedge on the retroside. All of the analogue FEM and DEM models presented here follow this scheme but not all reach stage 3.

2.2.1. Sandbox Models

[13] Dry sand has been used extensively as an analogue for brittle deformation of the upper crust in the Earth's field of gravity. This section is not intended to form a comprehensive review of sandbox modeling, it focuses on three specific applications of the technique which will be discussed later in the paper. The angle of internal friction is just over 30° and the apparent cohesive strength is approximately 1.05 kPa. It has been shown that sand exhibits Navier-Coulomb behavior similar to many sedimentary rocks [*McClay*, 1990]. Importantly, a layer of sand several centimeters thick can deform easily under its own weight, satisfying the scaling laws for body forces and surface forces. Faults that form within the models are not discrete fractures, but granular shear zones of finite width proportional to their grain size and form by progressive dilation. They can now be imaged in scanners without the model being destroyed to obtain a three-dimensional (3-D) time evolution.

[14] The properties of sand are complicated. *Krantz* [1991] noted that the density of a portion of sand is more dependent upon its physical handling than composition, and that the internal friction coefficient varies significantly depending upon the tightness of the packing. This makes it difficult to directly compare the work of different groups
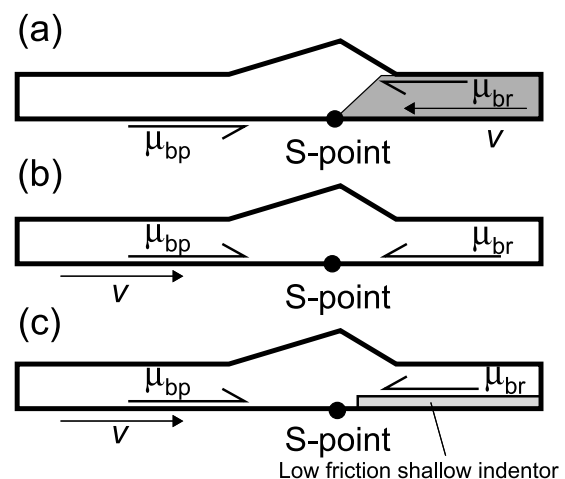

(a)
μ_{br}
μ_{bp} S-point v

(b)
μ_{bp} μ_{br}
v S-point

(c)
μ_{bp} μ_{br}
v S-point
Low friction shallow indentor

Figure 3. Boundary conditions for various doubly vergent sandbox experiments. The parameter v indicates the direction of convergence; μ_{bp}, μ_{br} and their corresponding half arrows indicate the presence proside and retroside basal friction. (a) Rigid indenters of various tapers intruding into deformable sand layer [*Persson*, 2001]. The frame of reference in this experiment has the subducting plate stationary with the retroside indenter and S point migrating into it. (b) Homogeneous medium with a weaker retroside base. Kinematic discontinuity is produced by drawing a sheet under the proside and drawing it out at the S point [*Malavieille*, 1984; *Storti et al.*, 2000], in this frame of reference the S point and over riding plate are stationary. (c) Homogeneous medium with a weaker retroside shallow indenter [*Wang and Davis*, 1996]. In this frame of reference the S point and overriding plate are stationary.
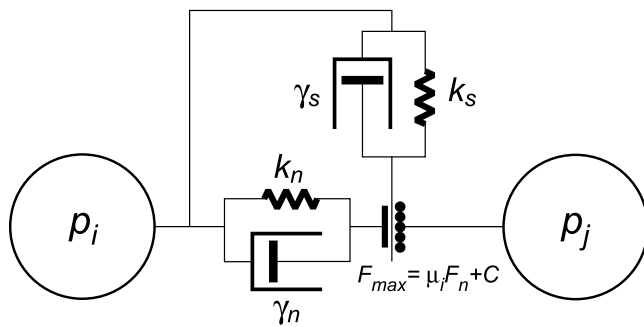
Figure 4. Spring dashpot model, a schematic representation of the p_ith to p_jth particle-particle contact forces applied in the discrete element model. The normal and tangential spring constants and damping coefficients are k_n, k_s and γ_n, γ_s, respectively. $F_{\max}$ is the Coulomb failure limit.

unless precise detail of experimental setup are given. Reactivated faults showed lower coefficients of friction in sand. Dilation in fault zones can be up to 13% [*McClay*, 1990], significantly larger than fault zones found in nature. *Koyi* [1995] saw individual imbricate sheets exhibit an area loss of 12–13% during shortening in his sandbox experiments. The elastic strain range of sand is significantly smaller than found in brittle rocks which makes it unsuitable for investigating seismic events.

[15] *Persson* [2001] used an analogue sandbox model to investigate how indenter geometry affected the rise of an orogenic wedge from an indented continent and observed stage 1 and 2 deformation (Figure 3a). A retrovergent thrust, which rises steeply from the S point and shallows toward the surface, was strongly localized near the S point. When the angle of the indenter was approximately the same as the angle of the retrovergent thrust, the thrust utilized the ramp. If the angle of the indenter was too shallow, a retrovergent thrust initiated at the base of the indenter with a steeper angle, partitioning a region adjacent to the indenter which is not further deformed. A steep indenter required the S point to step back from the toe of the indenter so that the thrust initiated was coincident with the top of the indenter but with a shallower angle. What is clear from these experiments is the persistence of a self-organizing retrovergent thrust.

[16] Similar results were obtained in a homogeneous material with no indenter by *Malavieille* [1984] and *Storti et al.* [2000]. A basal velocity discontinuity (Figure 3b) was sufficient to produce a similar retrovergent structure. This suggests that the retrovergent structure was a result of a common kinematic effect as the presence of a stronger backstop is not a necessity for the formation of the structure. Both experiments effectively partition deformation across this structure so that no deformation occurs in the retrowedge and thus stage 3 is never reached.

[17] *Wang and Davis* [1996] introduced a weak surface above a shallow backstop in the retrowedge to simulate the growth of thin-skinned contractional wedges over a strong backstop (Figure 3c). Experiments were performed for different basal coefficients of friction on the backstop's upper surface (μ_{br}). Weak surfaces on the backstop allowed deformation to propagate to the retroside, i.e., stage 3 growth. This suggests that the friction between the sand and the retrobase in the other experiments was too strong to

allow progression to stage 3. However, in the above case the indenter introduced is of a finite height and potentially introduces a further geometric complication that hinders a direct comparison with the other sand-box models [*Malavieille*, 1984; *Storti et al.*, 2000].

2.2.2. Finite Element Models

[18] Finite element models (FEMs) have been applied to critical wedge and doubly vergent systems. They have provided insight into the dynamics and controls upon such systems and allowed a full investigation of parameter space. They have also made it possible to investigate more complex feedbacks and couplings due to processes such as erosion [*Willett*, 1999], isostasy and temperature-dependent rheology which were not previously accessible. They resolve the gross form and first-order structures, such as the dominant retrovergent thrust in sandbox models. However, due to the assumption that the material deforms as a continuum, they find it difficult to resolve finer structures and must be forced to allow discrete thrust sheets to evolve [e.g., *Beaumont et al.*, 2000].

[19] *Willett et al.* [1993] outlined a boundary arrangement for investigating doubly vergent wedges at active margins or during continent-continent collision. *Beaumont et al.* [1996] further developed this idea to vary the proportions of incoming material incorporated into the wedge versus that subducted.

3. Discrete Element Method

[20] The discrete element method (DEM) was first described by *Cundall and Strack* [1979] as an application to granular assemblies. DEMs have been used to investigate the properties of granular shear zones [*Morgan and Boettcher*, 1999; *Morgan*, 1999], the propagation of blind thrusting has been tackled in two dimensions by *Finch et al.* [2003] and in three dimensions by *Strayer and Suppe* [2002]. A numerical simulation of seismic waves using a discrete particle scheme was performed by *Toomey and Bean* [2000] with the aim of developing a tool to investigate wave propagation in multiphase media. They have also proven particularly useful in studies of granular materials where the bulk properties emerge as a result of individual contact interactions and their histories at a finite scale. Recent work has produced FEM-DEM coupled models to study the interaction of particles suspended in a gas or liquid flow [*Limtrakul et al.*, 2003].

[21] Elements can represent either discrete objects, such as individual grains of sand, or bulk materials. In the experiments presented in this study, each element represents some mass of rock. The particle sizes define the resolution of structures within the model. They will allow a full exploration of parameter space appropriate to geological and sandbox problems and have the potential to self organize structures.

3.1. Contact Forces

[22] The spring dashpot model, illustrated schematically in Figure 4, is applied to determine contact forces between the ith and jth discs, with centroid locations (x_i, y_i), (x_j, y_j) and radii R_i, R_j. The normal repulsive force is proportional to the amount of overlap, δ_n at the contact (Figure 5a) and the tangential component is proportional to the amount of
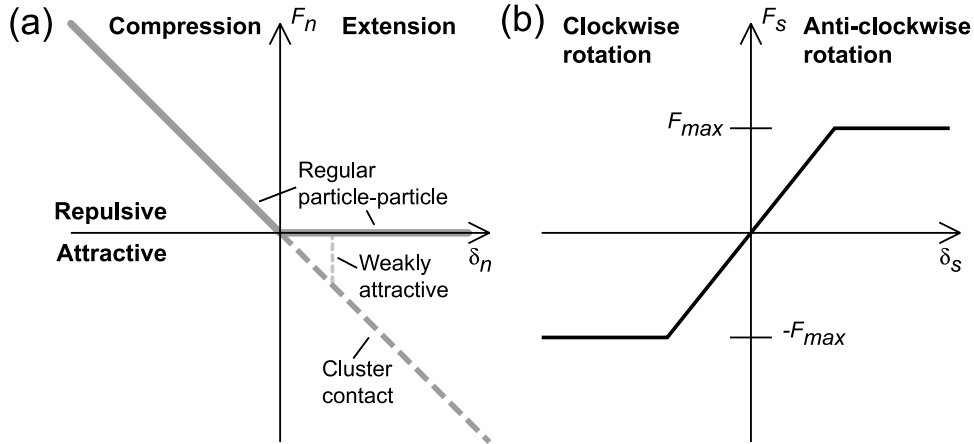
Figure 5. Force versus displacement laws for normal and tangential components of particle contact force. (a) Normal force which is purely repulsive under compression. Clusters of discs forming aggregate particles have strong attractive forces under extension. (b) Maximum tangential force which is limited by a Coulomb failure criterion which is proportional to the Normal contact force.

tangential displacement, δ_s since the contact was formed (Figure 5b).

[23] For each contact, relative displacements are given by

$$\delta_n = \sqrt{(x_i - x_j)^2 + (y_i - y_j)^2} - (R_i + R_j)$$
$$\delta_s = \delta_t - R_i\delta_{\theta_i} - R_j\delta_{\theta_j} \qquad (1)$$

where δ_t is the cumulative tangential translation and $\delta\theta_q$ the rotation of the qth particle since the contact was formed. This introduces a history-dependent factor into the force evaluation.

[24] If the particles overlap, they are within the normal force limit $\delta_n < 0$, and

$$F_n = -k_n\delta_n \qquad (2)$$

$$F_s = -k_s\delta_s \qquad (3)$$

or else

$$F_n = F_s = 0$$

The frictional tangential force is limited by a Coulomb failure threshold, above which sliding occurs. The limit is proportional to the magnitude of the normal force, such that stronger contacts resist more sliding.

[25] If $|F_s| > F_{\max}$, then

$$|F_s| = |F_{\max}|$$

where $F_{\max} = F_n \tan \phi_i + C$. Here ϕ_i is the internal angle of friction parameter and C the cohesion (Figure 4). If all of the contacts are at Coulomb failure, information about the deformation history would be lost from the tangential contact force term.

[26] The nature of the contact interaction force can be varied to give the material different properties (Figure 5a). For instance, by extending the range of the normal force

limit $\delta_n < 0$ to infinity, pairs of rigid particles can be formed. Alternatively a weak perturbation could be added so that once an initial contact is broken new contacts only interact repulsively, thus preferential motion along preexisting fault planes is incorporated, i.e., strain weakening. Damping is used to increase the numerical stability of the model, but an under damped contact force could be employed to simulate a viscous material. The flexibility of the contact force law formulation provides an opportunity to address some of the problems of the release of elastic strain energy and especially the associated nonlinear effects within thrust wedges noted by *Bombolakis* [1994].

[27] The most computationally intensive process in running a DEM is contact detection. If we were to compare every particle with every other particle, the speed of the program scales approximately with the square of the number of particles. To avoid this, we can linearly sort the particles into a cell structure by their x and y coordinates [*Allen and Tildesley*, 1987], storing this information in a Linked List. Then we only need compare particles in adjacent cells. Forces are equal and opposite, so we need only compare Cell A with Cell B and not the reverse.

3.2. Boundary Conditions

[28] A number of DEM experiments have been investigated as part of this study. Here, we describe the terminology used in the experimental setups. Rigid walls interact with particles using the same repulsive force law as the particle-particle interactions (Equation (2)), where the magnitude of the force is proportional to the overlap with the boundary. For a general wall, where the closest points to the ith particle are (x_b, y_b) the normal overlap is given by

$$\delta_n = \sqrt{(x_i - x_b)^2 + (y_i - y_b)^2} - R_i \qquad (4)$$

A smooth wall imparts no tangential force at its contacts. A rough surface allows a tangential component which resists motion parallel to the surface through a frictional
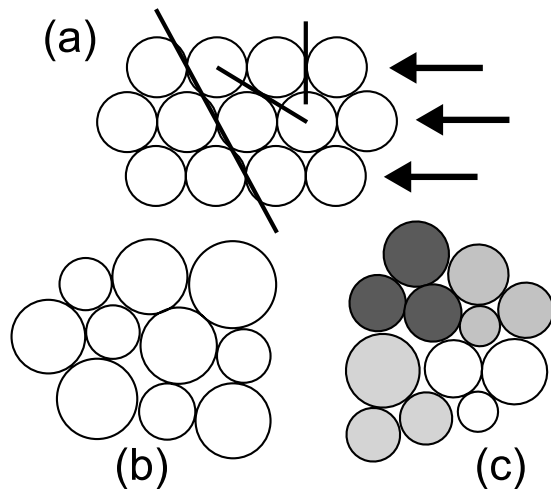
Figure 6. Particle packing structures investigated. (a) Regular hexagonal packing which has many predefined planes of weakness and linear chains of particles which can transmit information over large distances. Simulations run using this packing are controlled by the packing structure. (b) Random particle sizes and positions which produce wedge growth more consistent with that of the sandbox models but with low angles as deformation occurs through the highly efficient mechanism of rolling particles. (c) Use of random clusters of particles which removes the problems associated with rolling by increasing the angularity of the particles. The shading identifies particles.

force law. In this study a Coulomb failure criterion has been applied limiting the magnitude of the tangential component.

3.3. Bulk Material Properties

[29] Various workers have investigated the properties of DEM materials [*Ting et al.*, 1989; *Oger et al.*, 1998; *Jensen et al.*, 1999; *Lanier and Jean*, 2000]. Depending upon the nature of the contact interactions applied, DEM materials commonly exhibit properties analogous to those of granular materials. For instance, the strength of the packing and the force distribution within are dependent on the contact geometry, the tightness of packing and thus how the packing was formed [*Lanier and Jean*, 2000]. The classic example is the measurement of the angle of repose of a sand pile. The term angle of repose is ambiguous as there is no precise definition, it describes the angle at which a material will remain stable, but this angle depends upon how the experiment was performed. Different angles are measured depending upon whether the pile was grown from a point source or a carefully distributed growth pattern [*Geng et al.*, 2001]. It is therefore unsurprising that particle morphology also affects the behavior of the material through physical protrusions meshing together.

[30] Many workers [*Ting et al.*, 1989; *Oger et al.*, 1998] have investigated the response of the global friction angle of discrete element materials to variations in the internal coefficient of friction using a biaxial test, $\mu_i \equiv \tan \phi_i$. For small values of the internal coefficient, $\mu_i < 0.1$, a large variation in the global angle is observed. As μ_i is

increased, a plateau in the measured angle is reached. The height of this plateau is dependent upon the grain size distribution, grain morphology and how the experiment was performed. *Zhou et al.* [2001] extensively examined the response of the angle of repose of a 3-D mono sized sphere DEM sandpile, varying only the coefficients of friction in the material for constant boundary conditions and observed similar results.

[31] Frictional behavior of real materials is complicated because frictional behavior on surfaces takes place at the atomic level. Amongst other things, the frictional coefficient is dependent upon the normal pressure, relative tangential velocity, surface roughness and temperature.

[32] Particle geometry has a significant effect on the friction of a bulk granular material and is observed in DEM simulations [*Ting et al.*, 1989]. Spherical particles exhibit significantly lower friction than angular particles [*Mair et al.*, 2002], it is believed that this is due to spherical grains accommodating strain in a highly efficient manner through rolling. The frictional behavior of angular and spherical particles is distinct, this is in addition to any coefficient of friction that is specified in the contact force laws. To simulate real materials we must introduce angularity to mimic this real atomic detail. We experimented with different particle geometries and packings to minimize strain being accommodated through rotation.

3.4. Packing Arrangements

[33] In two dimensions, particles consist of one or more discs. The packing structures investigated different particle arrangements (Figure 6). An initial particle distribution is generated, and then allowed to settle under gravity to some equilibrium arrangement, before any experiments were performed. We compare the properties of these packing structures with the aid of singly vergent critical wedge experiments (Figure 7).

3.4.1. Regular Hexagonal Packing

[34] A regular hexagonal packing structure (Figure 6a) using discs of uniform size, has been employed to study accretionary wedges and fold-and-thrust belts [*Burbidge and Braun*, 2002]. This packing has predefined planes of weakness to shearing and artificial strength along long linear chains, which initiate pop-ups at a long distance from the toe of the wedge (Figure 7a). This packing is the most compact system, and thus any disruption weakens it. It was argued that the anisotropy in the layering would better simulate sedimentary packings, which are often layered, and facilitate strain weakening. We believe that the more fundamental behavior of a homogeneous material with no predefined planes of weakness or fault geometries should first be investigated. This is important in establishing which properties are a consequence of the boundary conditions and which from the packing arrangement. Subsequent experiments can then relate the structural evolution to this reference. Additionally, it would be useful if the degree of strain weakening along fault planes could be definable through some initial parameter; this cannot be achieved if strain weakening is employed as a function of the packing.

3.4.2. Random Single Disc

[35] To address some of the issues outlined above, a random medium was generated. This material consists of
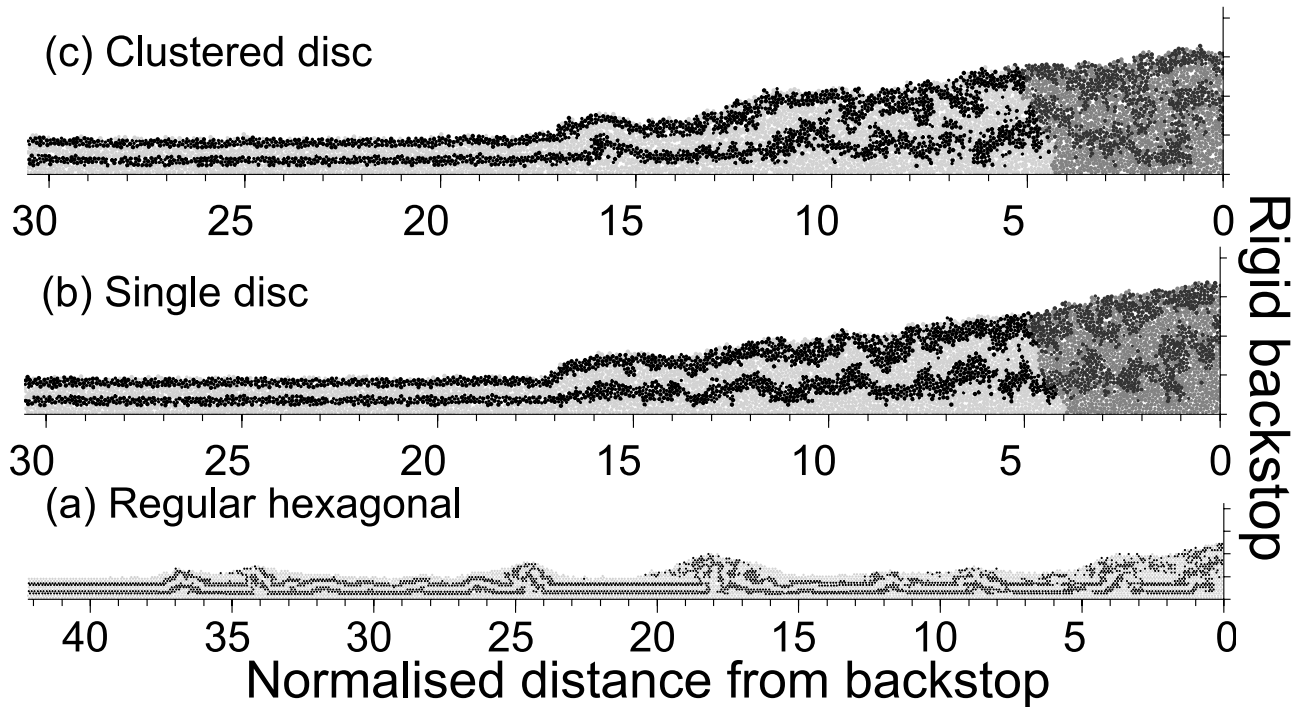
Figure 7. Results from three singly vergent critical wedge experiments performed using identical boundary conditions but varying the particle geometry and packing structure employed. (a) Regular hexagonal, (b) random single disc, and (c) random clustered disc.

discs with a random size, between limits, positioned randomly (Figure 6b). We found that this material immediately improved critical wedge-type growth over the regular hexagonal packing. A critical wedge was seen to form at the moving backstop with oscillations in the localization of deformation dependent upon the basal friction. However, the angle of the wedge was low due to discs frequently rolling and avalanching down the surface due to overrotation. Various methods have been identified to overcome this problem, which mainly focus on increasing particle angularity [*Ting et al.*, 1993]. This is done through more complex particle geometries including ovular and polygonal particles, these more complex shapes increase the time for contact detection which rapidly becomes more complicated for noncircular particles.

3.4.3. Random Clusters

[36] This study applied an alternative approach to tackling the problem of overrotation, proposed by *Jensen et al.* [1999]. Particles consisting of clusters of 3 random sized discs are used to increase angularity (Figure 6c). These particles remain intact for all time by redefining the contact force for clustered particles such that,

[37] For all δ_n

$$F_n = -k_n \delta_n$$

This scheme is a simple extension of the standard contact force law, the expense is in increasing the degrees of freedom for each particle by the number of discs in each particle. *Jensen et al.* [1999] used three regular sized particles to form an equilateral triangle; in our study the isotropic nature has been increased by using particles

made from three random sized discs, between limits, linked together in a triangular formation. This increased the material shear strength and reduced the particle rotation.

3.5. Dilation of Material

[38] Dilation is observed in sandbox analogues, as much as a 13% loss of volume in a bulk sample [*Koyi*, 1995]. This change in volume alters the strength of the packing and is a problem with the sandbox approach, but it is also why the material localizes deformation; experiments have been run to investigate this for the DEM. A time evolution of the volume of various wedges above a mean surface, as a percentage of the shortened volume, was investigated to check the dilation properties of the doubly vergent system.

[39] The area of the wedge above the undeformed surface, A_w, is compared with the area of accreted material, A_s. The model is divided into columns of constant thickness δ_x and a surface is defined by the maximum particle height, y_i, in each column. The area of the wedge is calculated by summing the areas of the columns that make up the wedge:

$$A_w = \delta x \sum (y_i - y_{mean})$$

The area of accreted material, A_s is given by the total amount of shortening, expressed as the product of the column width and the total number of columns accreted, ndx:

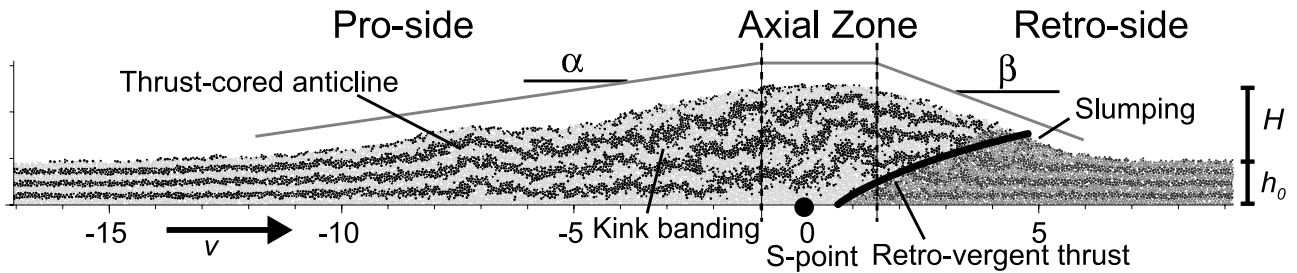$$A_s = ndx \, \delta x \, y_{mean}$$

Figure 8. Typical doubly vergent wedge DEM output for fixed retroside boundary condition arrangement, with some key features labeled. The basal velocity discontinuity (the change in convergence from v to 0) is introduced at the S point. The angles of the prowedges and retrowedges are α and β, respectively; the axial zone is the region over which the taper changes from α to β; h_0 is the mean undeformed depth of material to be accreted to the wedge; and H is the height of the wedge above the mean undeformed surface. Kink banding, as defined by *Malavieille* [1984], refers to the internal deformation, folding and faulting of the initial horizons.

Thus the percentage dilation is given by

$$D = \frac{A_w}{A_s} 100$$
$$= \frac{\sum y_i - y_{\text{mean}}}{ndx\, y_{\text{mean}}} 100$$

The initial trend is highly dependent upon the choice of the mean surface height so it is difficult to say whether the material is initially contracting or dilating, but regardless of the precise choice of mean surface height, as y_i becomes significantly greater than y_{mean} the ratio of the areas tends to a constant of about 95%. While dilation does provide a mechanism for strain weakening, we believe that the percentage dilation is small enough that it is not a primary control on the mechanics of the system.

4. Doubly Vergent Wedges

[40] We shall present a series of experiments to demonstrate the validity of the DEM approach, first by applying different boundary conditions and second by investigating controls on the macroscale development of doubly vergent wedges. The experimental boundary conditions are intended to be equivalent to two infinite slabs colliding at the S point. Random cluster particles are used as these best represent crustal material. Each model consists of ~10,000 particles. Much of the following work is discussed in terms of the normalized convergence (i.e., total convergence normalized by the mean thickness of the incoming, undeformed material, h_0). This scale is interchangeable with time assuming a constant convergence rate, v. The zero intercept marks the velocity discontinuity at the S point. By nondimensionalizing the problem in this way, we can compare the model output with real wedges on different time and length scales.

4.1. Model Visualization and Output

[41] The model outputs snapshot data at regular time intervals. These record the positions and instantaneous velocities of particles within the system. The particle positions are plotted using GMT, and colored to highlight different features of interest. Here we present models colored by initial depth below the surface to show the deformation of horizontal markers and colored by the maximum displacement of each particle relative to its neighboring particles (between the previous and next output time steps) to pick out the persistent structures over a given time interval.

5. Development of Lower Boundary Conditions

[42] Two different lower boundary conditions are presented to illustrate how the DEM doubly vergent wedge systems relate to sandbox analogues, FEM models and real systems. Both boundary condition formulations use a Coulomb base on the proside moving at a constant velocity with respect to the S point, generating a traction force acting on the elements overlying this boundary. The first boundary condition is used in Experiments 1 and 2 where all elements in contact with the retroside lower boundary are fixed in space (see section 5.1). This produces a very high retroside basal friction and compare well with sandbox experiments which use rigid indenters. Experiments 1 and 2 investigate the response of the wedge to variation in proside basal friction and internal friction, respectively. Experiment 3 uses a Coulomb retroside base and varies retroside basal friction, producing a wedge more consistent with the FEM simulations (see section 5.2).

[43] The traction force ($F_{traction}^i$) applied to the proside tends the velocity (v^i) of the ith particle in contact with the lower boundary to the subduction velocity (v') where

$$F_{traction}^i = \gamma\left(v^i - v'\right) \qquad (5)$$

This is only one term added to the force summation, so the particle can still fail on the boundary. For the addition of this term to allow stable solutions, the maximum displacement (δ_e) it induces in a given time step must be smaller than the maximum permissible overlap of two particles (δ_n):
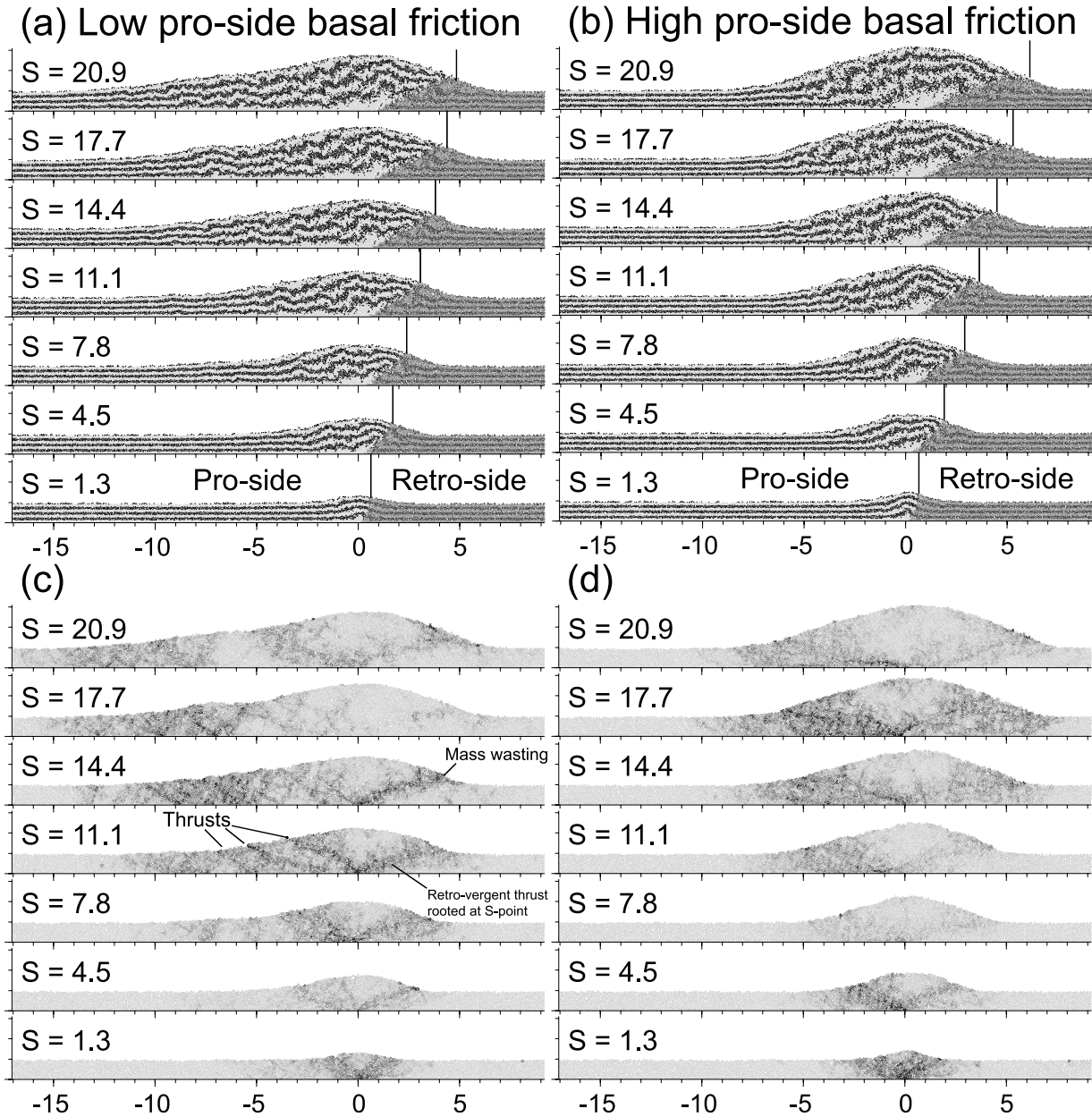
$$\delta_e < \delta_n \qquad (6)$$

Figure 9. Images of DEM doubly vergent wedge experiment results using the fixed retroside boundary condition for experiment 1. (a) and (b) Comparison of the deformation of initially horizontal horizons. The higher basal friction ($\mu_{bp} = 0.5$) supports a steeper proside wedge. The darker shaded retroside material is pinned at the S point. (c) and(d) Maximum relative displacement of adjacent particles, scaled to the maximum value over each interval, for the fixed retroside experimental boundary condition. The lower basal friction ($\mu_{bp} = 0.1$) allows the deformation to propagate further into the proside. The position along the x axis is normalized by the thickness of the material with the origin at the S point. A strongly localized retrovergent structure is localized, also pinned at the S point.

For a constant convergence rate $v' = \dfrac{\delta e}{dt}$. From equation (2), $\delta_n = \dfrac{mg}{k_n}$. Therefore from equation (5), v' must satisfy

$$v' < \frac{mg}{k_n\,dt}$$
$$< \frac{\pi R^2 \rho\,g}{k_n\,dt}$$

5.1. Fixed Retroside Boundary Condition

[44] Some of the typical features of the mature experimental output obtained using lower boundary conditions with a fixed retroside are highlighted in Figure 8. Two main wedges form either side of an axial zone. The retrowedge is steep and is formed by the flux of material through the wedge and the slumping of material down the surface at some angle of repose, β, while the prowedge has a shal-

(a)

Height of wedge vs. normalised convergence

(b)

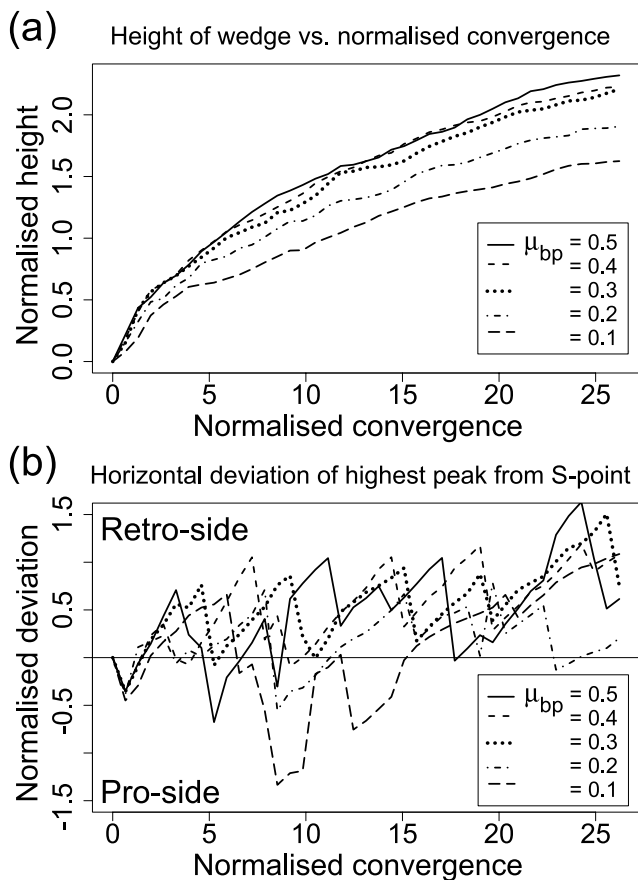Horizontal deviation of highest peak from S-point

Figure 10. (a) Maximum height and (b) deviation of highest point from S point versus normalized convergence, S per unit model depth for experiment 1 with a range of proside basal friction values, μ_{bp} = 0.1–0.5. All length scales are normalize by the mean thickness of accreted material. The height of the wedges increases approximately with $S^{\frac{1}{2}}$, in a relatively smooth curve. The position of the highest peak oscillates rapidly around some point near the S point and advects slowly to the retroside.

lower taper, α, reflecting its accretionary growth mechanism. Taper angles are calculated by fitting a straight line through the centroids of the particles forming the upper surface of each wedge at a particular time. A strong retrovergent thrust is rooted at the singularity (gray line) and tends to the retroside surface at the tip of the retrowedge. This retrovergent thrust effectively decouples the prosides and retrosides and pins retroside material at the S point. Pop-up structures can sometimes be seen to develop beyond the tip of the prowedge before being incorporated. Retroside friction is an emergent property of the interaction of the fixed retroside particles with the material above. The fixed particles have less degrees of freedom than the free particles, thus the friction along this contact must be greater than the emergent bulk material friction.

5.1.1. Experiment 1: Variation in Proside Basal Friction, μ_{bp}

[45] Keeping the internal angle of friction constant and relatively high (μ_i = 0.3), we varied the proside basal coefficient of friction, μ_{bp} relative to the retroside. The

asymmetry in the basal friction is reflected in the asymmetry of the gross morphology and strain history (Figure 9). Lower values of basal friction cause the proside deformation front to propagate further from the S point. Higher values made the prowedge narrower, and made the gross form more symmetric about a vertical plane approximately above the S point. To sustain this symmetry for successive accretion on the proside, motion is required on the retro-verging thrust. Thus the evolution of the retrowedge is dependent on the basal friction on the proside.

[46] The rate of growth of the wedges decreases with convergence (Figure 10a) due to a constant flux of material being added to an ever larger wedge. Higher basal frictions produce steeper sided wedges, thus to accommodate the same shortening the wedge must be higher. The lateral deviation of the highest peak, the point of greatest elevation across the wedge from the S point, fluctuates rapidly around the S point (Figure 10b), but a general trend of advection of the highest peak toward the retroside can be seen; a similar
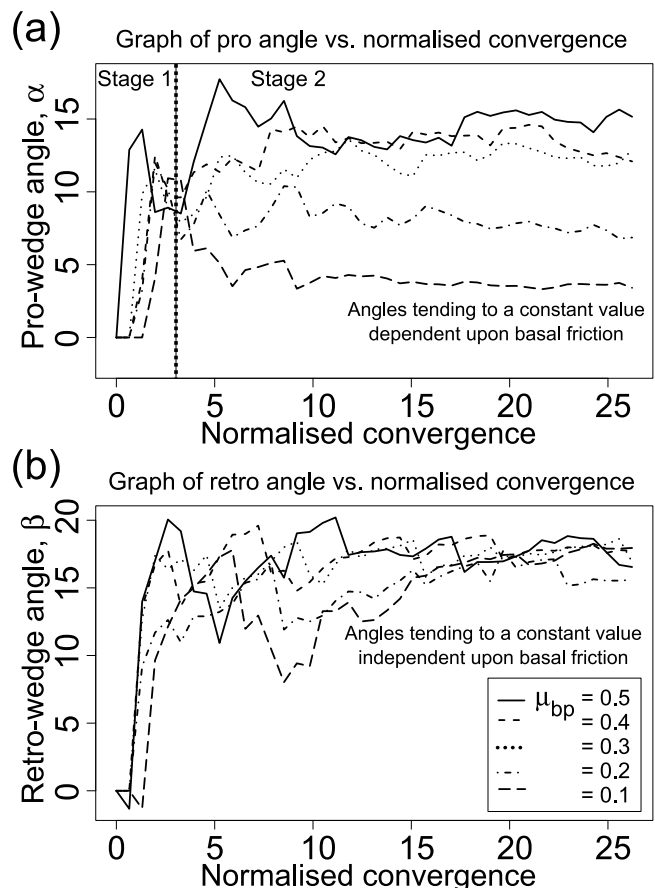
(a)

Graph of pro angle vs. normalised convergence

(b)

Graph of retro angle vs. normalised convergence

Figure 11. Angles of the (a) prowedge and (b) retrowedge versus total convergence per unit depth for experiment 1 with a range of proside basal friction values, μ_{bp} = 0.1–0.5. All length scales are normalize by the mean thickness of accreted material. After an initial period of similar growth where the wedges fail internally, the angles of the prowedge tend to some limit dependent upon the proside basal friction. In contrast, the retrowedge angles all tend to the same limit.
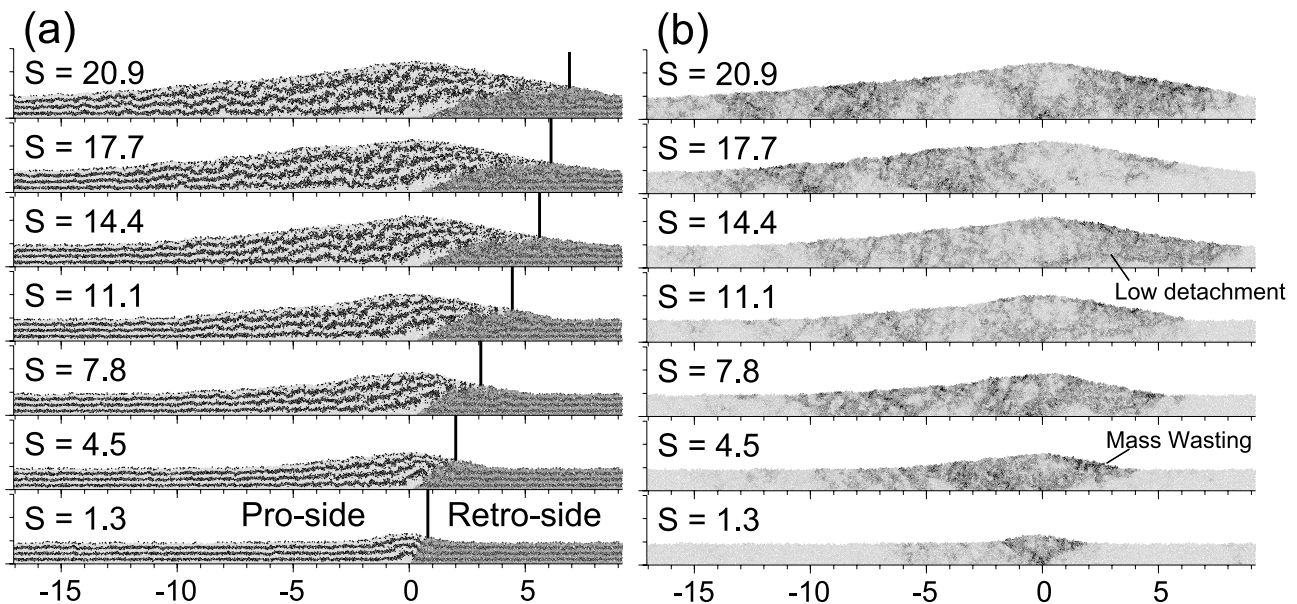
Figure 12. Images of DEM doubly vergent wedge experiment results using the fixed retroside boundary condition for experiment 2. (a) and (b) Comparison of the deformation of initially horizontal horizons and the maximum relative displacement of adjacent particles for the fixed retroside experimental boundary condition with low internal and basal friction. The lower internal friction angle produces wedge angles more similar to those in orogens. The higher angles in Figure 9 are more akin to sandbox models. Notice the high amount of relative motion along the wedge surfaces suggesting that slumping is an important process in these experiments. The position on along the x axis is normalized by the thickness of the material with the origin at the S point.

result is seen in FEM experiments [*Willett*, 1999]. It appears that lower basal angles of friction produce less deviation of the highest point from the S point.

[47] Initially, the angle of all the prowedges, α, increase in the same manner to a similar angle for a normalized convergence of $S \approx 3$ (Figure 11a). After this they diverge to a value dependent upon the proside basal friction. Lower basal frictions produce shallower tapers. The initial similar increase in α is due to stage 1 growth where the wedge does not yet require support on the base and thus α is independent of the basal friction and is more a function of the properties of the material. The retrowedge angle, β, attains the same plateau angle for all values of basal friction. The retrowedge angle is steeper than the angle of the prowedge as it is not formed by an accretionary mechanism. Material in the wedge is fluxed through to the retroside and the angle of the retrowedge is limited by some angle of repose of the system. Evidence for this is the presence of slumped material at the base of the retrowedge. It is important to note that retrowedge accretion, and hence the development of stage 3, is not achieved in these experiments.

[48] Figures 9c and 9d show the maximum displacement of neighboring particles. The initial block uplift bound by two shear zones is evident at $S = 1.3$ for both series. Lower basal friction produces more clearly separated discrete structures. This is especially evident when you compare the prosides later in the experiments. The retrovergent thrust is resolved in both experiments, but again it is clearer in the case of lower basal friction. The slumped material on the retroside is also highlighted, indicating that this process is

on the same order of magnitude as the motion along structures.

5.1.2. Experiment 2: Variation in Internal Friction, μ_i

[49] We repeated Experiment 1 for the case with low basal friction, this time reducing the internal friction of the DEM material (Figure 12). The angle of the retrowedge was lower this time due to the lower internal strength, as are the shear zones that bound the initial block uplift of stage 1. The increased proportion of slumping on both the retrowedge and prowedge is highlighted in Figure 12b. For the same basal friction and relative shortening, the deformation has propagated further to the proside. Interestingly, while still pinned at the S point, the retrovergent thrust becomes less localized though still remaining clearly discrete, and forms a lower detachment in the retroside at later stages in its evolution.

5.1.3. Summary of Results of Fixed Retroside Boundary Condition

[50] These results show a similar evolution to the sandbox experiments that do not reach stage 3 retrowedge accretion [*Malavieille*, 1984; *Storti et al.*, 2000; *Persson*, 2001]. All experiments saw retroside deformation initiate at the S point, but it did not propagate further along the base. The retrovergent thrust is pinned at the S point and it partitions the deformation. A significant amount of material is seen to slump down the retrowedge, giving this surface a uniform taper angle. Higher proside basal frictions inhibit stable sliding on the proside base, the shortening being accommodated through diffuse internal deformation within the prowedge. Lower proside basal frictions allow the deformation
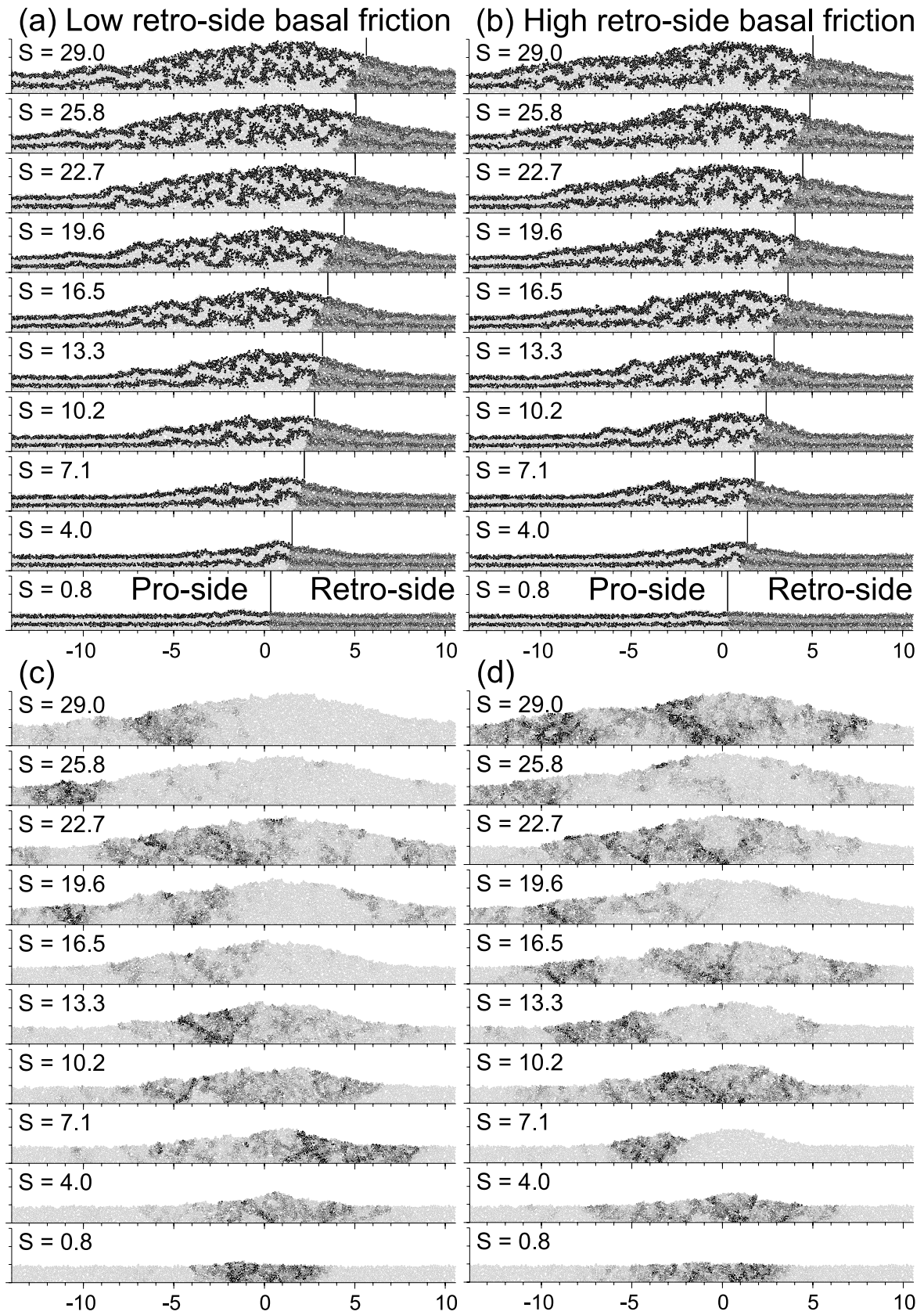
Figure 13

to be accommodated on more discrete structures at greater distances from the S point. In all experiments, the axial zone remains relatively undeformed and grows in size as deformation shifts further to the prosides and retrosides.

5.2. Coulomb Retroside Boundary Condition

[51] The use of a Coulomb retroside lower boundary reduces the retroside boundary friction and allows it to be defined.

5.2.1. Experiment 3: Investigating the Role of Retroside Basal Friction

[52] The retroside basal friction was increased by different factors relative to the proside basal friction. Deformation now propagates into the retroside and the whole wedge is able to slide stably on both the probases and retrobases. This can be seen by the advection of retroside material away from the S point (Figure 13). The retrovergent thrust is no longer pinned at the S point. The angle of the steep retrowedge is relatively insensitive to the retroside basal friction as this angle is some angle of repose, primarily limited by the internal strength of the material (Figure 14b). Less slumping occurs on this surface now as there is a second mechanism to accommodate shortening on the retroside. As the whole wedge slides stably, a shallower accretionary wedge forms beyond the toe of the steep retrowedge. The extent of this wedge is limited by retroside basal friction (compare Figures 13c and 13d). The prowedge and retrowedge angles shown in Figures 14a and 14b are averages over the whole prowedge and retrowedge and do not highlight the breaks in slope due to pop-ups at the toe of the prowedge and accretion of retroside material into the retrowedge. As might be expected, higher values of μ_{br} encourage accretion purely on the proside toe with the retrowedge preserved at a steep taper. Lower values allow deformation to propagate into the retroside basin, with a shallow wedge accreting onto the tip of the steep retrowedge. For the range of retroside basal frictions investigated ($\mu_{br} = 2, 5, 10 \mu_{bp}$), all the wedges grow vertically with similar rates (Figure 15a). We now see spikes in both the prowedges and retrowedges as they reach their thresholds upon which they require support on the base (Figures 14a and 14b). The retrowedge reaches this threshold later than the prowedge.

[53] The highest peak is seen to advect gradually toward the retroside before suddenly switching to a newly formed peak on the proside (Figure 15b), oscillating approximately two mean thicknesses, h_0 either side of the S point; this has important implications for the advection of topography and drainage capture across the drainage divide of mountain belts ([e.g., the Landsborough River, Southern Alps, New Zealand [Koons, 1994]). This behavior is less erratic and more periodic than for the fixed retroside boundary con-

ditions as the wedge is now free to slide on the retroside base whereas before, deformation was forced to localize purely on the proside. The time evolution of the height of the wedge is also more periodic (Figure 15a), reflecting periodicity in the deviation of the highest peak. This suggests that for the Coulomb retroside boundary condition the deformation remains more localized over a given period of time, rather than constantly adjusting.

6. Summary and Discussion

[54] The two boundary conditions presented above simulate previous sandbox and FEM approaches. The first formulation has the retroside as being relatively passive with deformation pinned at the S point, overriding the retroside. The prosides and retrosides are relatively decoupled and weaker materials see deformation propagate deeper into the retroside. The second formulation sees deformation propagate into the retroside and retroside material is accreted to form a second shallower wedge.

6.1. Evolution of the Doubly Vergent System

[55] Our experiments have confirmed that doubly vergent wedge systems evolve through a three stage scheme [Willett et al., 1993] defined by the modes of deformation utilized to accommodate shortening. The boundary conditions applied to some sandbox experiments are such that the system never progresses to stage 3 deformation, that is, the accretion of retroside material. We discuss the nature of deformation exhibited in each stage and possible controls on the system which allow the system to enter the next stage.

[56] The key point is that there are thresholds within the system that must be attained before a new mode of deformation is required. Deformation across the wedge is distributed depending upon the extent of sliding along the base which in turn is controlled by friction parameters.

6.1.1. Stage 1

[57] Initially, two shear zones rooted at the S point initiate a V-shape block uplift by translating the plug to the retroside along the retroverging shear zone. The angle of these shear zones is strongly dependent upon the global strength of the material. It is this shear zone which develops into the dominant retrovergent thrust. This can be seen most clearly in Figure 9d at $t = 2$, although it does occur in all experiments.

[58] The duration of stage 1 is clearly highlighted in Figure 11a for a normalized convergence of less than 3, which shows that the angle of the prowedge is initially insensitive to proside basal friction until the wedge has reached a critical size beyond which the wedge requires support on the base.

Figure 13. Experiment 3 results using the Coulomb retroside boundary condition comparing the deformation of initially horizontal horizons under relatively (a) low ($\mu_{br} = 2\mu_{bp}$) and (b) high ($\mu_{br} = 10\mu_{bp}$) retroside basal friction. (c) and (d) Low and high basal friction, respectively, colored by the maximum relative displacement of adjacent material scaled to the maximum relative displacement between output time steps. Note how the retroside material, shaded darker, is no longer pinned to the S point and slides toward the retroside (compare Figure 9). A second, shallower wedge has developed beyond the steep retrowedge as material is accreted at the toe, the magnitude of retroside basal friction regulates the amount of material accreted in this manner. The position on along the x axis is normalized by the thickness of the material with the origin at the S point.
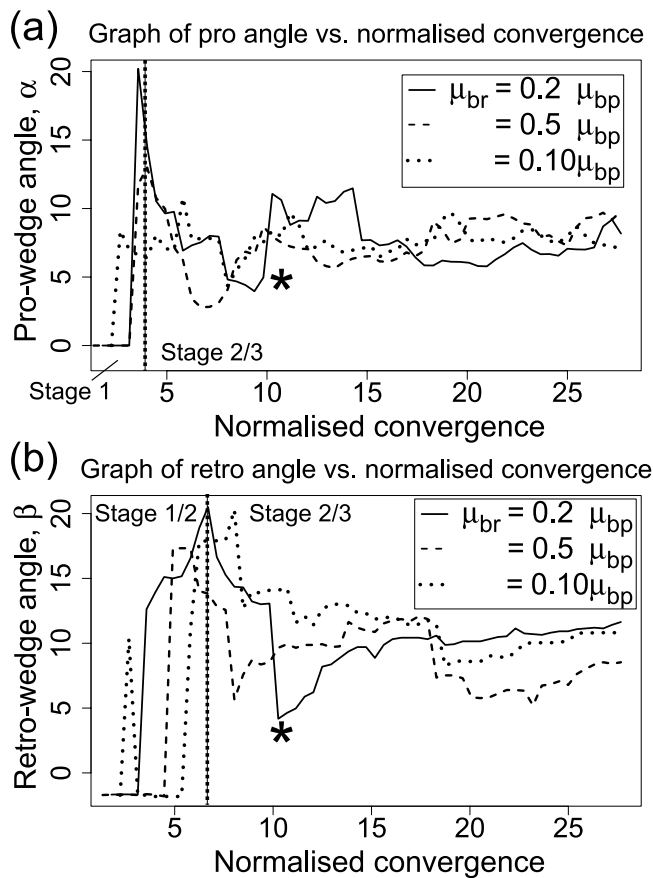
Figure 14. Angles of the (a) prowedge and (b) retrowedge versus total convergence per unit model depth for experiment 3 with different ratios of probasal to retro-basal friction, where μ_{br} = 2, 5, 10 μ_{bp}. There is now a spike in both the prowedge and retrowedge angles. These occur as the respective wedges start to fail on the lower boundary rather than internally. The prowedge angle is the first to deviate, and subsequently, the retroside starts to accrete material. The star highlights a specific event in Figures 14 and 15.

[59] All of the doubly vergent sandbox experiments described in section 2.2.1 formed the retrovergent thrust at an early stage. This suggests that the formation of a retrovergent thrust is a result of the kinematic boundary conditions present in both experiments, rather than the presence of a rigid indenter. The kinematic boundary condition provides the primary control on the system. The retrovergent thrust is a first-order structure that is observed in many settings, examples of which include the North Pyrenean Fault [*Fischer*, 1984], Insubric Line in the European Alps [*Pfiffner et al.*, 1997] and the Longitudinal Valley Fault of eastern Taiwan [*Hickman et al.*, 2002]. It is also well resolved in finite element models as regions of highly localized strain [e.g., *Willett et al.*, 1993].

6.1.2. Stage 2

[60] Deformation now propagates to the proside of the singularity as the wedge begins to slide stably on the proside base. The angle of the prowedge is now dependent upon the proside basal friction and departs from the initial trend (Figure 11a for normalized convergence >3) and is

formed through frontal accretion of foreland material. Once the initial transient response has died down, the angle remains relatively constant. The steeper retrowedge is formed by material fluxing through the wedge and its angle reflects some angle of repose of the system. Examples of the consequent topographic asymmetry include central Taiwan [*Deffontaines et al.*, 1994] and the Olympic Mountains of Washington State [*Pazzaglia and Brandon*, 2001].

[61] A low basal friction can only support a shallow proside wedge and new thrust sheets are seen to initiate beyond the toe of the wedge. A high basal friction localizes deformation nearer the S point as information cannot travel as far along the base. One can envisage a system in which as the wedge grows further, its weight is felt at greater depths and as this becomes coincident with deeper weak layers, a drop in detachment occurs; this would equate to a process of underplating.
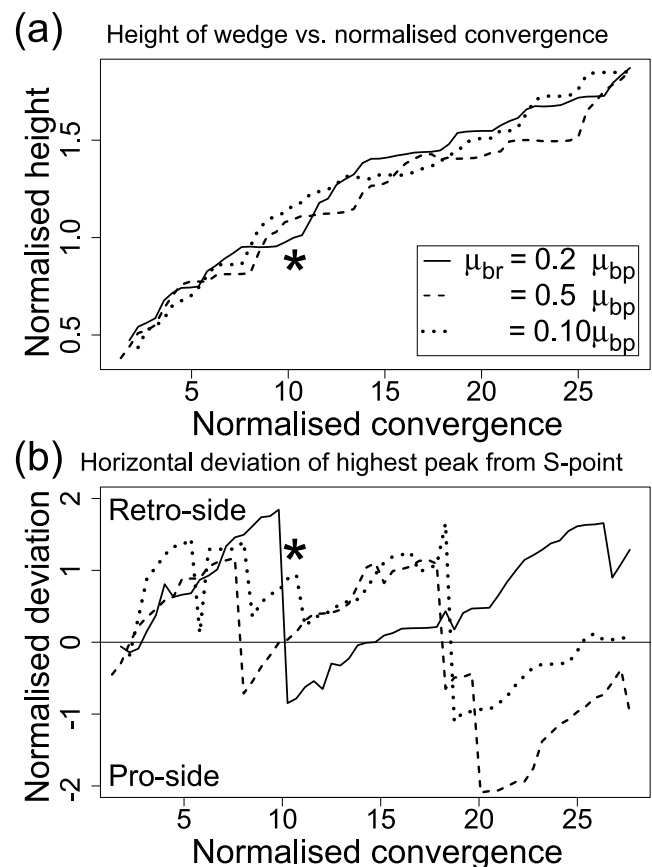

Figure 15. (a) Maximum height and (b) deviation of highest point from S point versus total convergence per unit model depth for experiment 3 with different ratios of probasal to retrobasal friction, where μ_{br} = 2, 5, 10 μ_{bp}. All length scales are normalize by the mean thickness of accreted material. The increase in height of the wedge and horizontal oscillation in the localization of the highest point relative to the S point is clearly episodic, with a longer time period. Deformation now remains localized in one region as compared with the fixed retroside boundary condition arrangements. There is a clear, gradual advection of the highest peak to the retroside before a rapid switch to a proside peak. The star highlights a specific event in Figures 14 and 15.

6.1.3. Stage 3

[62] Sliding on the retrobase is initiated and the deformation front propagates into the undeformed layer beyond the tip of the retrowedge and initiates the formation of a lower taper wedge. The initiation of sliding can be seen in Figure 14b where the initial spike in basal friction drops to a lower value once retroside accretion has been initiated. This second retrowedge is formed by material accreted onto the toe of the steeper retrowedge, its angle is lower as it is formed in an accretionary manner, not by a large flux of material as in the case of the steeper wedge.

[63] The experiments run under the first boundary condition do not permit sliding on the retroside base and this third stage is never reached. However, the formation of the deeper detachment in Figure 12b at $S = 7.8$ does suggest that if the experiments were to run for long enough, the models may accrete at the toe. The second boundary arrangement rapidly moved into stage 3 very soon after stage 2 had been reached. There is a large tolerance for the thresholds that control this transition.

6.2. Implications for Interpreting Real Systems

[64] Overall, these models highlight the importance of the mechanisms (e.g., frontal accretion, internal thickening) available to accommodate shortening in the topographic and kinematic evolution of doubly vergent wedges; the two boundary conditions employed in this study differ in this respect. The Coulomb retroside boundary condition shows strong coupling between topographic evolution and internal kinematics. The strongest evidence for coupling in the modeled data occurs for the Coulomb retroside boundary condition with the lowest relative retroside friction, and is marked with a star in Figures 15 and 14. This event corresponds to a change in position of the highest peak from the retroside to the proside. In moving the highest peak to the proside, we see a corresponding rapid steepening of the prowedge and a shallowing of the retrowedge in Figures 14a and 14b immediately followed by a gradual correction back toward the mean taper angles. In these simulations the highest peak illustrates the tectonic component of drainage divide migration. This tectonic coupling between topography and internal kinematics resulting in localized deformation with relatively slow rates of migration of the drainage divide away from the proside, related to the incorporation of successive thrust sheets. In contrast, migration of the drainage divide toward the prowedge occurs in relatively instantaneous events generated by localized uplift to the proside of the drainage divide; once the shift in position has taken place, the maximum height of the wedge starts to increase again, localized on the new drainage divide (Figure 15a). This process may comprise a tectonic component in catchment capture events in real systems such as has been suggested for the Landsborough River in the Southern Alps, New Zealand [*Tippett and Hovius*, 2000].

[65] The fixed retroside boundary condition did not permit stage 3 retroside accretion; a comparison of Figures 10 and 11 with Figures 15 and 14 shows less coupled behavior and more self similar growth for the fixed retroside boundary condition experiments. It is the ability of the wedge to exist in regimes where the processes to accommodate shortening differ, that allow deformation to be localized. For example, retrowedge accretion is the only efficient process available to shallow the retrowedge, without it the doubly vergent wedge can only accrete on the proside with the evolution of the retroside topography being controlled through slumping by its angle of repose.

7. Conclusions

[66] A new model has been developed to study controls upon the structural, kinematic and macrogeomorphic development of mountain belts using a discrete element technique. The development of a Coulomb retroside boundary condition is significant for investigating doubly vergent wedges, as it allows the basal friction to be specified rather than it being an emergent function of particle geometry and the internal coefficient of friction. The DEM provides a complimentary alternative to sand-box and finite element models of orogenesis. It extends the range of parameter space available to sand-box models and allows the emergent propagation of thrust structures which are poorly resolved, and frequently predefined, in FEMs.

[67] Experiments run using variable boundary conditions have allowed us to compare and contrast previous modeling approaches. Similar model outputs can be obtained for both a system with or without a rigid indenter (as used in some sand-box models), and that therefore the primary control on the system is the kinematic boundary conditions not rheological discontinuities.

[68] Topography and internal kinematics are strongly coupled by the processes available to accommodate shortening. There are thresholds in geometry and size that regulate the location, duration and mode of deformation (e.g., prowedge or retrowedge frontal accretion). In all experiments there is significant advection of proside material into the retrowedge. The retrowedge may comprise two sections; a more internal steep component generated by the thrusting of material through the wedge ramping on the first-order retrovergent thrust and a more external shallower wedge formed by accretion of the retroside. Material in the steep retrowedge has been fluxed from the prowedge to the retroside, this is confirmed by the presence of slumped material at the base of the retrowedge which shows that the slope is near some angle of repose of the material. Once the wedge has reached a threshold size, the Coulomb retroside boundary condition experiments develop a second shallower wedge accreting on the retroside as the retrodeformation front propagates out. Higher values of proside basal friction make the wedge more symmetric about the highest peak as the proside angle tends toward a similar angle of repose as the retroside.

[69] The topographic ridge is seen to oscillate around a point above the singularity. The experiments showed a gradual advection of the topographic ridge to the retroside, followed by a rapid switch in location to the proside as the deformation localized internally in order to sustain constant taper angles. This has important implications for drainage capture across a drainage divide.

References

Allen, M. P., and D. J. Tildesley (1987), *Computer Simulation of Liquids*, 2nd ed., Oxford Univ. Press, New York.

Beaumont, C., S. Ellis, J. Hamilton, and P. Fullsack (1996), Mechanical model for subduction-collision tectonics of alpine-type compressional orogens, *Geology*, 24(8), 675–678.

Beaumont, C., J. A. Munoz, J. Hamilton, and P. Fullsack (2000), Factors controlling the alpine evolution of the central Pyrenees inferred from a comparison of observations and geodynamical models, *J. Geophys. Res.*, 104, 8121–8145.

Bombolakis, E. G. (1994), Applicability of critical-wedge theories to foreland belts, *Geology*, 22, 535–538.

Burbidge, D. R., and J. Braun (2002), Numerical models of the evolution of accretionary wedges and fold-and-thrust belts using the distinct-element method, *Geophys. J. Int.*, 148, 542–561.

Chapple, W. M. (1978), Mechanics of thin-skinned fold-and-thrust belts, *Geol. Soc. Am. Bull.*, 89, 330–345.

Cundall, P. A., and O. D. L. Strack (1979), A discrete numerical model for granular assemblies, *Geotechnique*, 29, 47–65.

Dahlen, F. A. (1984), Noncohesive critical Coulomb wedges: An exact solution, *J. Geophys. Res.*, 89, 10,125–10,133.

Dahlen, F. A., J. Suppe, and D. Davies (1984), Mechanics of fold and thrust belts and accretionary wedges: Cohesive Coulomb theory, *J. Geophys. Res.*, 88, 10,087–10,101.

Davis, D., J. Suppe, and F. A. Dahlen (1983), Mechanics of fold and thrust belts and accretionary wedges, *J. Geophys. Res.*, 88, 1153–1172.

Deffontaines, B., J. C. Lee, J. Angelier, J. Carvalho, and J. P. Rudant (1994), New geomorphic data on the active Taiwan orogen: A multisource approach, *J. Geophys. Res.*, 99, 20,243–20,266.

Finch, E., S. Hardy, and R. Gawthorpe (2003), Discrete element modelling of contractional fault-propagation folding above rigid basement fault block, *J. Struct. Geol.*, 25, 515–528.

Fischer, M. W. (1984), Thrust tectonics in the northern Pyrenees, *J. Struct. Geol.*, 6, 721–726.

Geng, J., E. Longhi, R. P. Behringer, and D. W. Howell (2001), Memory in two-dimensional heap experiments, *Phys. Rev. E*, 64, 060301.

Heim, A. (1897), *Untersuchungen uber den mechanismus de Gebirgsbildung im Anschluss an die geologische Monographie der Todi-Windgallengruppe*, Schwabe, Basel, Switzerland.

Hickman, J. B., D. V. Wiltschko, J. H. Hung, P. Fang, and Y. Bock (2002), Structure and evolution of the active fold-and-thrust belt of southwestern Taiwan from Global Positioning System analysis, *Spec. Pap. Geol. Soc. Am.*, 385, 75–92.

Huiqi, L., K. McClay, and D. Powel (1992), Physical models of thrust wedges, in *Thrust Tectonics*, edited by K. McClay, pp. 71–81, CRC Press, Boca Raton, Fla.

Jensen, P. R., P. J. Bosscher, M. E. Plesha, and T. B. Edil (1999), DEM simulation of granular media-structure interface: Effects of surface roughness and particle shape, *Int. J. Numer. Anal. Methods Geomech.*, 23, 531–547.

Karner, G. D., and A. B. Watts (1983), Gravity anomalies and flexure of the lithosphere at mountain ranges, *J. Geophys. Res.*, 88, 10,449–10,477.

Koons, P. O. (1994), Three-dimensional critical wedges: Tectonics and topography in oblique collisional orogens, *J. Geophys. Res.*, 99, 12,301–12,315.

Koyi, H. (1995), Mode of internal deformation in sand wedges, *J. Struct. Geol.*, 17(2), 293–300.

Krantz, R. W. (1991), Measurements of friction coefficients and cohesion for faulting and fault reactivation in laboratory models using sand and sand mixtures, *Tectonophysics*, 188, 203–207.

Lanier, J., and M. Jean (2000), Experiments and numerical simulations with 2D disks assembly, *Powder Technol.*, 109, 206–221.

Limtrakul, S., A. Chalermwattanatai, K. Ungurawirote, Y. Tsuji, T. Kawaguchi, and W. Tanthapanichakoon (2003), Discrete particle simulation of solids motion in a gas-solid fluidized bed, *Chem. Eng. Sci.*, 58, 915–921.

Mair, K., K. M. Frye, and C. Marone (2002), Influence of grain characteristics on the friction of granular shear zones, *J. Geophys. Res.*, 107(B10), 2219, doi:10.1029/2001JB000516.

Malavieille, J. (1984), Modelisation experimentale des chevauchements imbriques: Application aux chaines de monta, *Bull. Soc. Geol. Fr.*, 7, 129–138.

McClay, K. R. (1990), Deformation mechanics in analogue models of extensional fault systems, in *Deformation Mechanisms, Rheology and Tectonics: Current Status and Future Perspectives*, edited by R. J. Knipe and E. H. Rutter, *Geol. Soc. Spec. Publ.*, 200, 445–453.

Morgan, J. K. (1999), Numerical simulations of granular shear zones using the distinct method: 2. The effect of particle size distribution and interparticle friction on mechanical behavior, *J. Geophys. Res.*, 104, 2721–2732.

Morgan, J. K., and M. S. Boettcher (1999), Numerical simulations of granular shear zones using the distinct element method: 1. Shear zone kinematics and micromechanics of localization, *J. Geophys. Res.*, 104, 2703–2719.

Munoz, J. A. (1992), Evolution of a continental collision belt: Ecors-Pyrenees crustal balanced cross-section, in *Thrust Tectonics*, edited by K. McClay, pp. 235–246, CRC Press, Boca Raton, Fla.

Nieuwland, D. A., J. H. Leutscher, and J. Gast (2000), Wedge equilibrium in fold and thrust belts: Prediction of out of sequence thrusting based on sandbox experiments and natural examples, *Neth. J. Geosci.*, 79(1), 81–91.

Oger, L., S. B. Savage, D. Corriveau, and M. Sayed (1998), Yield and deformation of an assembly of disks subjected to a devioric stress loading, *Mech. Mater.*, 27, 189–210.

Pazzaglia, F. J., and M. T. Brandon (2001), A fluvial record of long-term steady-state uplift and erosion across the Cascadia forearc high, western Washington State, *Am. J. Sci.*, 301, 385–431.

Persson, K. S. (2001), Effective indenters and the development of doubly vergent orogens: Insights from analogue sand models, in *Tectonic Modeling*, edited by H. A. Koyi and N. S. Mancktelow, *Mem. Geol. Soc. Am.*, 193, 191–206.

Pfiffner, O. A., P. Lehner, P. Heitzmann, S. Muller, and A. Steck (Eds.) (1997), *Deep Structure of the Swiss Alps: Results of PNR 20*, Springer, New York.

Platt, J. P. (1986), Dynamics of orogenic wedges and the uplift of high-pressure metamorphic rocks, *Geol. Soc. Am. Bull.*, 97, 1037–1053.

Storti, F., F. Slavini, and K. McClay (2000), Synchronous and velocity-partitioned thrusting and thrust polarity reversal in experimentally produced and doubly-vergent thrust wedges: Implications for natural orogens, *Tectonics*, 19, 378–396.

Strayer, L. N., and J. Suppe (2002), Out-of-plane motion of a thrust sheet during along-strike propagation of a thrust ramp: A distinct-element approach, *J. Struct. Geol.*, 24(4), 637–650.

Ting, J. M., B. T. Corkum, C. R. Kauffman, and C. Greco (1989), Discrete numerical model for soil mechanics, *J. Geotech. Eng.*, 115(3), 379–398.

Ting, J. M., M. Khwaja, L. Meachum, and J. Rowell (1993), An ellipse-based discrete element model for granular materials, *Int. J. Numer. Anal. Methods Geomech.*, 17, 603–623.

Tippett, J. M., and N. Hovius (2000), Geodynamic processes in the Southern Alps, New Zealand, in *Geomorphology and Global Tectonics*, edited by M. A. Summerfield, pp. 109–134, John Wiley, Hoboken, N. J.

Toomey, A., and C. J. Bean (2000), Numerical simulation of seismic waves using a discrete particle scheme, *Geophys. J. Int.*, 141, 595–604.

Wang, W. H., and D. M. Davis (1996), Sandbox model simulation of forearc evolution and noncritical wedges, *J. Geophys. Res.*, 101, 11,329–11,339.

Willett, S., C. Beaumont, and P. Fullsack (1993), Mechanical model for the tectonics of doubly vergent compressional orogens, *Geology*, 21, 371–374.

Willett, S. D. (1992), Kinematic and dynamic growth and change of a Coulomb wedge, in *Thrust Tectonics*, edited by K. McClay, pp. 19–31, CRC Press, Boca Raton, Fla.

Willett, S. D. (1999), Orogeny and orography: The effects of erosion on the structure of mountain belts, *J. Geophys. Res.*, 104, 28,957–28,981.

Zhou, Y. C., B. H. Xu, A. B. Yu, and P. Zulliq (2001), Numerical investigation of the angle of repose of monosized spheres, *Phys. Rev. E*, 64(02), 021301.

————————————
P. A. Cowie, M. Naylor, and H. D. Sinclair, School of GeoSciences, University of Edinburgh, Edinburgh EH9 3JW, UK. (mark.naylor@ed.ac.uk)

S. Willett, Department of Earth and Space Sciences, University of Washington, Seattle, WA 98195, USA.